Beam folding analysis and optimization of mask-enhanced toroidal multipass cells

MANUEL GRAF[1], HERBERT LOOSER[1,2], LUKAS EMMENEGGER[1], AND BÉLA TUZSON[1,*]

[1] Empa, Laboratory for Air Pollution/Environmental Technology, CH-8600 Dübendorf, Switzerland
[2] Institute for Aerosol and Sensor Technology, Fachhochschule Nordwestschweiz (FHNW), CH-5210 Windisch, Switzerland
[*] Corresponding author: bela.tuzson@empa.ch

Compiled July 19, 2017

We present computational and experimental investigations of the beam folding properties and fringe suppression capabilities in monolithic toroidal multipass cells when combined with absorption masks. Coherent field simulations based on Fresnel-Huygens theory were performed to understand the effect of multiple field truncations in such an optically semi-unstable mirror arrangement. The explicit numerical calculation of the radiation field at each reflection allows detailed optimization and performance analysis. We experimentally verified the evolving irradiance distributions and identified optimal initial field configurations. Furthermore, we suggest a proxy to estimate the noise level for specific initial conditions. These insights pave the way to a better optical performance and thus to even more lightweight and compact designs of this multipass cell type.

OCIS codes: *(120.0120) Instrumentation, measurement, and metrology; (300.1030) Absorption Spectroscopy; (080.2740) Geometric optical design; (080.2730) Matrix methods in paraxial optics.*

http://dx.doi.org/10.1364/ao.XX.XXXXXX

Trace gas analysis by means of direct absorption spectroscopy is a widely used technique and currently advances towards highly compact and mobile applications. High precision measurements at low mixing ratios require the extension of the optical path through the sampling volume, typically by means of a multipass cell (MPC). Driven by their mechanical simplicity, the most frequently applied concepts are all based on a coaxial arrangement of two mirrors [1], while specific mirror curvatures enhance the beam folding density [2, 3]. Motivated by the demand for portable and lightweight instrumentation, the concept of monolithic toroidal MPC has been proposed [4]. These cells can be designed very compact and versatile. Moreover, they are expected to operate well even under harsh environmental conditions, as their rotational symmetry enhances the tolerance against optical misalignment and pattern variation. In addition, the monolithic construction makes this concept exceptionally attractive for both mobile and mass-critical applications. Recently, toroidal MPCs were successfully applied in high precision atmospheric NO_2 measurements [5, 6] and real-time breath gas analysis [7]. The reported sub-ppb analytical precision, however, could only be achieved by inserting an aperture mask in the cell volume as schematically depicted in Fig. 1(a). Empirical investigations of such mask-enhanced toroidal multipass cells (MET-MPC) showed that this approach effectively reduces the optical fringe-noise. However, neither the physical reasons for this noise-suppression nor any strategies for further improvement and optimization have yet been reported.

This letter presents a computational approach to investigate the beam folding properties of such MET-MPCs. Extensive numerical simulation are performed to elucidate the key factors determining the optical performance of this type of MPC. We discuss the intensity evolution characteristics for varying initial conditions as well as their potential impact on the noise level.

The constructional concept of a toroidal multipass cell has been described in detail elsewhere [5]. Therefore, only the relevant elements for the subsequent stability discussion are briefly summarized here. The principle of toroidal MPCs is based on the emergence of a N-star polygram when a geometrical ray enters the cell under an angle θ with respect to its radial line (Fig. 1b). However, due to their coherent nature, physical laser beams differ from geometrical rays as they have both finite spatial extent and nonzero divergence. Thus, the mirror arrangement of a MPC must be suitable to conserve the beam shape upon many reflections. To investigate the beam stability, the subsequent reflections within a toroidal cell may be considered as a spatially distributed resonator, where each reflection is a few degrees rotated with respect to the center of the MPC. Applying paraxial matrix-methods, one finds the relation between curvature and displacement of mirrors that allows the stable propagation of light over many reflections [8]. The beam stability can be analyzed separately in two perpendicular planes [9]: the horizontal (or tangential, xz) and the vertical (or sagittal, yz) plane as indicated Fig. 1(a). The mirror curvature along the vertical axis is unconstrained and can be freely chosen e.g. to fulfill the beam stability criterion, which states that the mirror separation L and their curvature radius R_y must compare as $L < 2R_y$ (e.g. confocal: $R_y = L$). In contrast, the curvature in the horizontal plane is given by the continuous revolution around the central axis of the cell. Hence, in the horizontal plane, the mirror curvature R_x is equal to the cell radius R_c and the distance between the

mirrors L of an equivalent resonator is *always* given by $L = 2R_c$. This corresponds to a *concentric* mirror arrangement, which is located at the border of the set of stable solutions in the resonator stability diagram [8]. As a result, Gaussian beams of any kind will diverge in the horizontal plane as they are reflected within this geometry. Thus, even after a small number of passes, single reflections cannot anymore be distinguished. In this case, the radiation that is leaving the cell towards the detector corresponds to a superposition of beam components which have experienced different numbers of reflections and thus traveled unequal distances. The resulting phase difference of these components manifests as undesired intensity modulations of the observed signal (fringes) as the laser wavelength is tuned. This effect has been observed experimentally [4] and it was significantly diminished by the insertion of an aperture-mask, which truncates the beam at each reflection [5]. Such a beam truncation not only reduces the transmission, but the successive generation of complicated diffraction patterns limits the ability to calculate beam characteristics and spectroscopic performance.

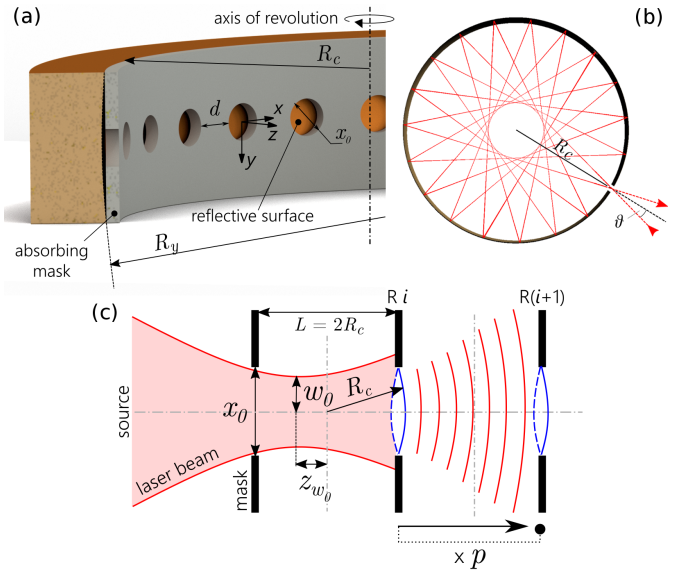

Fig. 1. (a) Cut through a toroidal cell indicating the main dimensions as well as the local coordinate system at the apertures. (b) Top-view onto the horizontal plane of a toroidal MPC where a geometric ray-trace simulation visualizes the beam path. (c) A schematic of the coherent wave propagation simulation, showing only the horizontal plane. For computation, the reflections in the cell are sequentially unfolded along a single axis: The initial Gaussian beam is focused such that the waist w_0 is located z_{w_0} away from the center of the first pass. After a potential clipping at the very first aperture, the radiation propagates to the opposite side of the cell where it is evaluated. Subsequently, the complex field is reflected on the toroidal mirror as well as truncated at the aperture of diameter x_0, followed by a propagation through free space of length L. The latter steps (truncation – reflection – propagation) are successively repeated p times in order to compute the complex radiation field at each reflection. Each time, the previously calculated field serves as initial distribution for the next pass.

To optimize the relevant dimensions of such a cell, as well as to find the optimal initial field, we simulated the propagation of coherent radiation within the toroidal geometry including a cylindrical mask of circular apertures. This problem is similar to an astigmatic resonator cavity with finite mirror size. Investigation of unstable resonator cavities [9, 10] revealed the emergence of steady-state solutions after many round-trips, characterizable by the Fresnel-number of the resonator [11]. For toroidal MPCs, however, the number of reflections is often too small for a stable mode to establish, and the energy-losses during this convergence process are more important than the properties of the steady state solution itself. Since the field structure depends significantly on the initial wave distribution during convergence, the complex field after each pass has to be calculated explicitly.

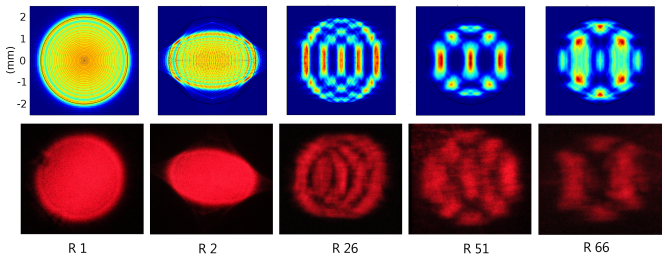

Fig. 2. (a) Comparison of the calculated (top) and the experimentally observed (bottom) irradiance distributions after different numbers of passes R i. The slight skew and rotation on the photographs is due to the non-perpendicular camera angle.

To simulate the wave propagation within MET-MPCs, we used the combination of Fresnel-Huygens (FH) theory with the paraxial ABCD-matrix formalism, allowing the propagation of arbitrary radiation fields within the limits of the Fresnel-approximation [8]. Since both cell- and aperture-diameter are large compared to the wavelength λ, the Fresnel-approximation is generally fulfilled for any geometry of practical interest. According to the FH-principle, the complex radiation field u_{i+1} is described as the superposition of waves emerging from each point of an earlier wavefront u_i:

$$u_{i+1}(\mathbf{r}_2) = \frac{i}{|\mathbf{B}|^{1/2}\lambda} \int_{-x_0/2}^{x_0/2} K(\mathbf{r}_1, \mathbf{r}_2) u_i(\mathbf{r}_1) \mathrm{d}\mathbf{r}_1 \qquad \textbf{(1)}$$

The effective optical distance of each of these waves is accounted for by adapting the FH-kernel $K(\mathbf{r}_1, \mathbf{r}_2)$ with the entries of the ABCD-matrix for the corresponding optical system. The astigmatic mirror curvature in two dimensions is described by a 4×4-matrix consisting of the four 2×2-matrices $\mathbf{A}$, $\mathbf{B}$, $\mathbf{C}$ $\mathbf{D}$, each containing the entries for both dimensions on their diagonal (cf. Eq. 2) [8, 12]. The numerical solving of the FH-integral (Eq. 1) for arbitrary systems on a Cartesian grid was implemented in Python.

Within MET-MPCs, the radiation is reflected on the concave astigmatic mirror with $R_x = R_c$ and R_y. At the same time, the aperture truncates the field, which is realized by setting the absorbed field-values to zero. Subsequently, the remaining radiation propagates through free space of length L, as illustrated in Fig. 1(c). Therefore, in one dimension, the ABCD-matrix describing this optical system is given by

$$M = \begin{bmatrix} 1 & L \\ 0 & 1 \end{bmatrix} \begin{bmatrix} 1 & 0 \\ -2/R_x & 1 \end{bmatrix} = \begin{bmatrix} 1 - \frac{2L}{R_x} & L \\ -\frac{2}{R_x} & 1 \end{bmatrix} \qquad \textbf{(2)}$$

Except for the very first mask-interaction, where the field experiences only a clipping and no phase variation, these steps are

repeated p times to acquire the radiation field at each reflection. Single-mode Gaussian beams were taken as initial fields. For clarity and unless otherwise stated, the reflectivity of the toroidal mirror was set to 100%. Generally, we assumed the incoupling angle θ to be small such that 3rd order astigmatism is negligible.

For the experimental assessment of this approach, we used a gold coated toroidal cell of horizontal radius R_c = 72 mm and vertical radius R_y = 131.6 mm. The incident angle θ was chosen to yield an optical path length of 9.9 m. The reflected light was clipped by a mask comprising 69 apertures of diameter x_0 = 4 mm. On this setup we also compared the calculated irradiance pattern with the experimental observation using a red trace laser (λ = 660 nm). Fig. 2 shows the excellent agreement between simulation and experiment after different numbers of reflections.

The successful verification allows to use this method for optimization calculations. Generally speaking, MPCs are designed to reach high transmission, long optical path length, and a low fringe-noise level. For mobile and compact instrumentation, this should be achieved with minimal weight and within a small volume. Often, these requirements are inherently exclusive: For instance, the overall transmission becomes higher if the apertures are larger, but at the cost of fewer reflections within a cell of equal diameter. These conceptual trade-offs have to be considered within the given constraints of the specific application. Therefore, we firstly focus on optimizations for a fixed representative geometry by assessing the impact of the initial field.

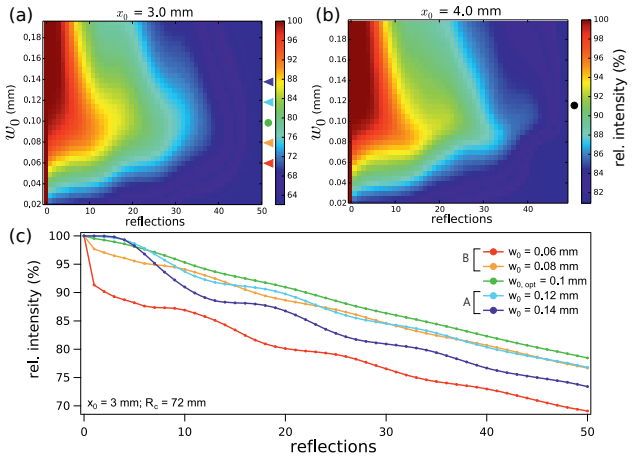

Fig. 3. Evolution of the relative residual intensity for different initial Gaussian beams as the radiation is successively reflected and truncated within the MET-MPC. For this one dimensional calculation of the unstable horizontal plane we assumed a cell with 72 mm radius and an aperture size of (a) 3 mm and (b) 4 mm for 6 μm wavelength of the laser. The optimal initial field, i.e. the one which leads to lowest intensity loss, is indicated with a bullet. (c) Horizontal slices (indicated by a triangle) through the left colormap highlight the intensity evolution structure for the two non-optimal regimes A and B.

In the stable vertical plane, the initial field can be chosen to match the eigenfunction of the corresponding geometry in order to minimize the clipped portion of the field. In contrast, finding optimal settings in the unstable horizontal plane is not trivial, since beam truncation cannot be avoided and the effect of any deviation from such an optimal case is non-intuitive. The intensity evolution is illustrated for two aperture sizes in Figs. 3(a) and (b) as a function of differently diverging Gaussian beams. Thereby, the initial field is fully defined by the laser wavelength and the beam-waist size, which is located at the center of the first pass. In order to highlight the influence of the unstable horizontal direction, the calculation was performed in one dimension, comprising only the horizontal axis. As expected, the transmission is generally higher in Fig. 3(b) than in Fig. 3(a) due to the 1 mm larger aperture-diameter. In addition, the dependence of the intensity evolution on the chosen initial field changes remarkably. However, similar tendencies are observed: Generally, we can identify two regimes of distinct loss-structure within the set of differently diverging Gaussian beams $u(w_0, \lambda)$ characterized by

$$\text{A)}\ w_0 > w_{0,opt} \quad \text{and} \quad \text{B)}\ w_0 < w_{0,opt} \tag{3}$$

The specific Gaussian initial field $u(w_{0,opt}, \lambda)$ yields the highest relative intensity for large numbers of reflection and decreases almost linearly. Furthermore, we expect $u(w_{0,opt}, \lambda)$ to minimize the fringe-level, since the diffraction-caused field spillover onto neighboring apertures is reduced. Therefore, it is referred to as the optimal initial field. The corresponding intensity evolution is labeled with a bullet in Fig. 3(a) and (b), and it is clearly dependent on the aperture-size. It turns out that the irradiance field $|u(w_{0,opt}, \lambda)|^2$ at the first aperture is most similar to that of the eigenfunction of an equivalent resonator and converges to it within a few reflections. If the initial Gaussian field deviates into range A, where the beam diameter is smaller than the first aperture, the intensity-loss follows a damped oscillation as the field converges to the steady state solution. In range B, the stronger divergence leads to a significant intensity-loss already at the very first aperture. This initial clipping at the input aperture can lead to an accentuated widespread diffraction at the first pass. Overall, the results clearly suggest that the beam waist w_0 should be chosen as $w_{0,opt}$ for best performance of the MPC. However, $w_0 > w_{0,opt}$ may be acceptable since the intensity loss and thus the diffraction-caused spillover are only slightly larger in total. For arbitrary dimensions of a toroidal cell, the optimal initial field at the first aperture can be estimated as *the* Gaussian beam with the smallest w_0 that yields an irradiance field most similar to the steady state solution. This resonator eigenmode may be found e.g. by the herein used successive approximation method, or the method of kernel expansion [9].

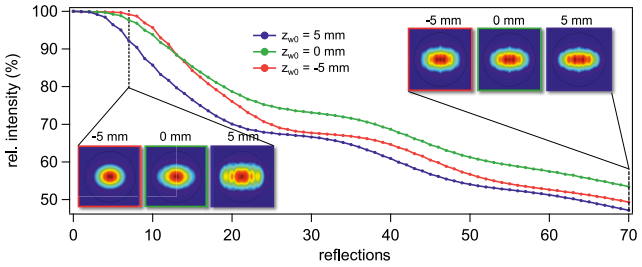

Fig. 4. (a) Normalized intensity evolution from a two dimensional calculation with λ = 4.3 μm, R_c = 72 mm, and circular apertures with diameter x_0 = 4 mm. The initial Gaussian field has a fixed waist size (w_0 = 0.1 mm) but is placed at three different positions z_{w_0}. Additionally, the irradiance patterns are compared for reflections R7 and R70.

Another significant impact on the intensity evolution can be attributed to the beam waist position of the first pass. Classical

geometrical considerations suggest the focus to be optimal if placed at the center between the entrance-aperture and the first reflection. The explicit simulation quantifies this dependence, and it furthermore reveals the self-similarity of the intensity evolution curves upon a waist displacement of $|z_{w_0}|$ (Fig. 4). If the waist is located *behind* the center (i.e. closer to the first reflection, $z_{w_0} = -5$ mm) a few reflections are needed to widen up the beam until the aperture interaction becomes dominant. While this leads to significant differences in the field shape at early reflections (cf. irradiance fields of R7, Fig. 4 insets left), the fields become indistinguishable after many round-trips (R70, insets right). Thus, the transmission of MET-MPCs can be optimized by centering the focus position, thereby avoiding unnecessary intensity-losses at early reflections.

By applying the computationally deduced optimal Gaussian beam configuration in the experimental setup mentioned above, we were able to lower the fringe-noise level from 4% [5] to 0.14%.

A complete geometrical optimization of MET-MPCs – including the optical path length as a variable – requires the quantification of the expected noise level and its dependence on the cell dimensions, particularly on the aperture-distance d. Multipass cells for absorption spectroscopy are often limited by optical fringes attributable to radiation falling onto the detector after having passed a different path length [13]. Although fringes typically occur between parallel semi-transparent surfaces in the optical path (etaloning), diffracted radiation leaking onto neighboring apertures causes a comparable effect within MET-MPCs. To a certain extent, these spillovers exist at each reflection. However, an absolute treatment by tracing all leaking radiation is not feasible. Therefore, we estimated the expected fringe-induced noise level considering the interference on the outgoing radiation by the neighboring fields. This was done by simulating all complex fields explicitly and superposing the last field together with the radiation spilling over from its direct neighbors onto the terminating aperture. Fig. 5(a) shows the calculated last field as well as the ones to its right and left, i.e. reflection 28 and 41, for the experimental setup described above. In general, the intensity of two superposed fields is given at each point by

$$I(\mathbf{r}) = I_1(\mathbf{r}) + I_2(\mathbf{r}) + 2\sqrt{I_1(\mathbf{r})I_2(\mathbf{r})}\cos(\phi_2(\mathbf{r}) - \phi_1(\mathbf{r})) \qquad \textbf{(4)}$$

and the total intensity is retrieved by integration over the entire aperture. As the wavelength is tuned, the local phase difference $\phi_2(\mathbf{r}) - \phi_1(\mathbf{r})$ changes, leading to an intensity modulation referred to as fringe-noise. Along these lines, we estimated the fringe level as the maximal intensity difference obtainable by an independent phase-variation of both interfering fields. This is plotted in Fig. 5(b) as function of the aperture distance d. Prior to this calculation, the relative intensity of the involved fields was scaled according to their reflection number, whereby a mirror reflectivity of 98% was assumed. We observe the intensity variation to decrease quickly and level off as the aperture distance increases. This is not only due to low peripheral intensity, in addition, the high spatial frequency of the phase far from the center leaves the total intensity almost unchanged upon variation of the phasor. For the experimental aperture distance $d = 2.6$ mm and diameter $x_0 = 4$ mm, this method predicts a fringe-induced relative variation of the integrated intensity of 0.7×10^{-4}, which cannot fully account for the measured optical noise level in the corresponding experiment (1.4×10^{-3}) as discussed above. This leads to the conclusion that the spillover at other apertures in the cell significantly contributes to the total observed fringe level. Nevertheless, the data suggest that for this particular setup and wavelength, a similar noise level can be expected for much smaller spacing of the apertures. Therefore, a corresponding adaption of the mask could increase the optical path length by more than a factor of two for the same cell size.

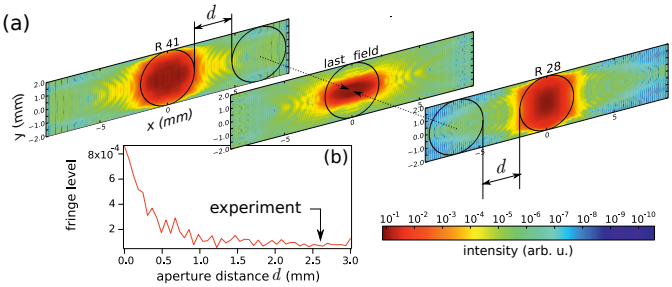

Fig. 5. The last irradiance field (R69) and its neighbors (R41 and R28) in logarithmic scale. To estimate the interference induced by diffracted radiation from neighboring fields, the superposition of these three fields is calculated within the last aperture. An independent phase variation of both interfering fields allows to retrieve the maximal intensity modulation upon laser wavelength tuning and is therefore a proxy for the fringe-caused noise level. This maximal modulation, normalized by the average intensity, is shown in (b) for different aperture distances d.

In conclusion, we discussed the inherent optical instability and demonstrated a strategy to optimize the performance of mask-enhanced toroidal multipass cells (MET-MPC). By explicit simulation of the complex radiation fields after each reflection, we showed the pseudo stabilization of the laser beam as a result of the successive clipping at the aperture mask. The influence of this truncation on the transmitted energy is presented for exemplary cases, and the simulation is used to predict optimal initial field configurations. We finally assessed the mutual interference of diffracted radiation from neighboring apertures as an important source of optical fringes. Thereby, we revealed further optimization potential towards more compact constructions. This supports MET-MPCs as lightweight and efficient alternatives to established strategies of beam folding.

Funding. Financial support was provided by the Swiss National Science Foundation (SNSF); Project No. 157208.

REFERENCES

1. D. Herriott, H. Kogelnik, and R. Kompfner, Appl. Opt. **3**, 523 (1964).
2. J. A. Silver, Appl. Opt. **44**, 6545 (2005).
3. J. B. McManus, P. L. Kebabian, and M. S. Zahniser, Appl. Opt. **34** (1995).
4. B. Tuzson, M. Mangold, H. Looser, A. Manninen, and L. Emmenegger, Opt. Lett. **38**, 257 (2013).
5. M. Mangold, B. Tuzson, M. Hundt, J. Jágerská, H. Looser, and L. Emmenegger, J. Opt. Soc. Am. A **33**, 913 (2016).
6. P. M. Hundt, M. Müller, M. Mangold, B. Tuzson, P. Scheidegger, H. Looser, C. Hüglin, and L. Emmenegger, Atmospheric Measurement Techniques Discussions **2017**, 1 (2017).
7. R. Ghorbani and F. M. Schmidt, Appl. Phys. B Lasers Opt. **123** (2017).
8. A. E. Siegman, *Lasers* (University Science Books, 1986).
9. H. Kogelnik and T. Li, IEEE J. Proc. **54**, 1312 (1966).
10. A. E. Siegman, Appl. Opt. **13**, 353 (1974).
11. A. G. Fox and T. Li, Bell Syst. Tech. J. **40**, 453 (1961).
12. M. Nazarathy and J. Shamir, J. Opt. Soc. Am. **72**, 356 (1982).
13. J. B. McManus and P. L. Kebabian, Appl. Opt. **29**, 898 (1990).

FULL REFERENCES

1. D. Herriott, H. Kogelnik, and R. Kompfner, "Off-Axis Paths in Spherical Mirror Interferometers," Appl. Opt. **3**, 523 (1964).
2. J. A. Silver, "Simple dense-pattern optical multipass cells," Appl. Opt. **44**, 6545–6556 (2005).
3. J. B. McManus, P. L. Kebabian, and M. S. Zahniser, "Astigmatic mirror multipass absorption cells for long-path-length spectroscopy," Appl. Opt. **34** (1995).
4. B. Tuzson, M. Mangold, H. Looser, A. Manninen, and L. Emmenegger, "Compact multipass optical cell for laser spectroscopy," Opt. Lett. **38**, 257–9 (2013).
5. M. Mangold, B. Tuzson, M. Hundt, J. Jágerská, H. Looser, and L. Emmenegger, "Circular paraboloid reflection cell for laser spectroscopic trace gas analysis," J. Opt. Soc. Am. A **33**, 913–919 (2016).
6. P. M. Hundt, M. Müller, M. Mangold, B. Tuzson, P. Scheidegger, H. Looser, C. Hüglin, and L. Emmenegger, "Spectroscopic real-time monitoring of no_2 for city scale modelling," Atmospheric Measurement Techniques Discussions **2017**, 1–21 (2017).
7. R. Ghorbani and F. M. Schmidt, "Real-time breath gas analysis of CO and CO2 using an EC-QCL," Appl. Phys. B Lasers Opt. **123** (2017).
8. A. E. Siegman, *Lasers* (University Science Books, 1986).
9. H. Kogelnik and T. Li, "Laser Beams and Resonators," IEEE J. Proc. **54**, 1312–1329 (1966).
10. A. E. Siegman, "Unstable optical resonators," Appl. Opt. **13**, 353–67 (1974).
11. A. G. Fox and T. Li, "Resonant Modes in a Maser Interferometer," Bell Syst. Tech. J. **40**, 453 – 488 (1961).
12. M. Nazarathy and J. Shamir, "First-order optics—a canonical operator representation: lossless systems," J. Opt. Soc. Am. **72**, 356 (1982).
13. J. B. McManus and P. L. Kebabian, "Narrow optical interference fringes for certain setup conditions in multipass absorption cells of the Herriott type," Appl. Opt. **29**, 898–900 (1990).